

Journal Pre-proof

Inertial amplification band-gap generation by coupling a levered mass with a locally resonant mass

Arnab Banerjee, Sondipon Adhikari, Mahmoud I. Hussein

PII: S0020-7403(21)00364-7
DOI: <https://doi.org/10.1016/j.ijmecsci.2021.106630>
Reference: MS 106630



To appear in: *International Journal of Mechanical Sciences*

Received date: 9 April 2021
Revised date: 22 June 2021
Accepted date: 26 June 2021

Please cite this article as: Arnab Banerjee, Sondipon Adhikari, Mahmoud I. Hussein, Inertial amplification band-gap generation by coupling a levered mass with a locally resonant mass, *International Journal of Mechanical Sciences* (2021), doi: <https://doi.org/10.1016/j.ijmecsci.2021.106630>

This is a PDF file of an article that has undergone enhancements after acceptance, such as the addition of a cover page and metadata, and formatting for readability, but it is not yet the definitive version of record. This version will undergo additional copyediting, typesetting and review before it is published in its final form, but we are providing this version to give early visibility of the article. Please note that, during the production process, errors may be discovered which could affect the content, and all legal disclaimers that apply to the journal pertain.

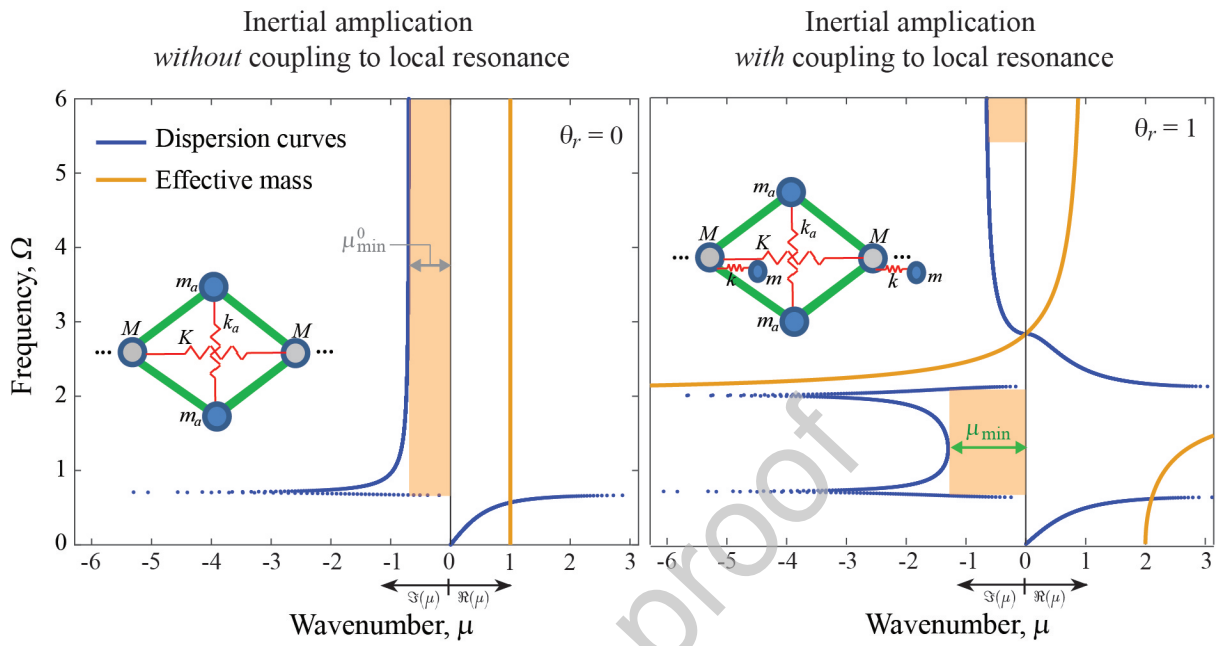
© 2021 Published by Elsevier Ltd.

1 **“Inertial amplification band-gap generation by coupling a levered mass with a locally resonant mass” by Banerjee et al.**

Highlights

- Novel concept for the realization of an inertial amplification band gap with double attenuation peaks
- Key feature: attenuation mode of the local resonance mass couples with the inertially amplified resonance leading to coupled double peaks in the attenuation profile
- Outcome: a combination of low frequency broadband gap, and strong spatial attenuation
- Three inertial amplification band-gap metrics introduced to characterize the band-gap size and attenuation properties, and optimization study performed.
- Results show a trade-off between double-peak band-gap width and minimum attenuation strength

2 Graphical Abstract





Inertial amplification band-gap generation by coupling a levered mass with a locally resonant mass

Arnab Banerjee^a, Sondipon Adhikari^b, Mahmoud I. Hussein^{c,d}

^a*Department of Civil Engineering, Indian Institute of Technology Delhi, India*

^b*College of Engineering, Swansea University, Swansea, UK*

^c*Smead Department of Aerospace Engineering Sciences, University of Colorado Boulder, Colorado, USA*

^d*Department of Physics, University of Colorado Boulder, Colorado, USA*

Abstract

Inertial amplification has been utilized in phononic media as a mechanism for the generation of large band gaps at low subwavelength frequencies. A unique feature in an inertial-amplification band gap is that it may exhibit two coupled peaks in the imaginary wavenumber portion of its band diagram. This unique double-attenuation band gap has been shown to emerge from a periodic arrangement of a levered mass whose motion is directly connected to that of an independent degree of freedom in the system through the motion of the lever base. Here we demonstrate a double-attenuation band gap emerging from a modal coupling of the levered mass with a conventional local-resonance mass separately attached to the base. This presents a fundamentally distinct mechanical mechanism for the shaping of inertially-amplified band gaps and provides a pathway for realising a combination of strength and breadth in the wave attenuation characteristics. We theoretically present this concept, analytically identify critical conditions for the coupling of the attenuation peaks, and provide a series of parametric sweeps to further highlight the phenomenon and guide design. For example, we find a design with a relatively elevated level of minimum attenuation over practically the entire width of a band gap with a relative size of 130%, and another design with a smaller band gap but a 15-fold increase in the minimum attenuation strength compared to a pure IA chain..

© 2021 Published by Elsevier Ltd.

Keywords: elastic metamaterials, inertial amplification, local resonance, band gaps, elastic waves, vibration attenuation

1. Introduction

The generation of frequency band gaps (stop bands) within which waves spatially attenuate is one of the coveted characteristics of periodic structures [1–3]. This concept has attracted research from a variety of disciplines, including vibrations, structural dynamics, acoustics, and materials physics. In an attenuation band, a free or driven wave cannot

Email addresses: abanerjee@iitd.ac.in (Arnab Banerjee), s.adhikari@swansea.ac.uk (Sondipon Adhikari), mih@colorado.edu (Mahmoud I. Hussein)

33 propagate, and instead experiences exponential attenuation along the direction of propa-
34 gation. The most common band-gap formation mechanism is based on wave interferences
35 and Bragg scattering. Destructive interferences of transmitted and reflected waves from
36 periodic inclusions, interfaces, and/or boundaries within the medium is the main cause
37 behind Bragg scattering [4, 5]. Band gaps may also emerge due to local resonances;
38 these may be realized in an elastic or acoustic waveguide with intrinsically embedded or
39 attached resonators (usually distributed periodically) [6, 7]. The key mechanism for lo-
40 cally resonance band gaps is a coupling—a hybridization—between substructure resonance
41 modes and elastic wave modes in the hosting medium.

42 Given the practical benefits of band gaps, it is often desirable to find unit-cell configu-
43 rations that exhibit band gaps that are both as low and wide as possible in the frequency
44 domain; see, for example, Refs. [8–12] for Bragg band gaps and Refs. [13–15] for local-
45 resonance band gaps. Band-gap enlargement by possibly utilizing more than one band-gap
46 mechanism in a combined manner has also been pursued [16, 17]. Relatively wide Bragg
47 band gaps may be realized by careful unit-cell topology design and optimization [8–10];
48 however, the unit cell is fundamentally constrained to be on the order of the wavelength of
49 the interfering waves. This, in turn, implies relatively high-frequency band gaps for small
50 unit cells. On the other hand, while local resonances provide an effective path towards
51 realizing low-frequency, subwavelength band gaps with small unit cells (since resonance
52 couplings are independent of wave interferences), these tend to be overly narrow and re-
53 quire a relatively heavy resonator to drop significantly in the frequency domain [18]. To
54 address these limitations, the mechanism of inertial amplification has been introduced as
55 an alternative for band-gap generation in structured media [19–21]. Inertial amplification
56 represents a contrast to local resonance in a subtle manner because it involves a mechan-
57 ical mechanism to provide a magnification of the “effective inertia” of a resonator. This
58 concept has been realized by the introduction of a lever-arm effect whereby the inertia
59 of a resonating mass is magnified to a degree proportional to the arm length. A unique
60 feature that emerges in certain implementations is the existence of a double-peak in the
61 attenuation profile which is represented in the imaginary part of the dispersion diagram
62 [22]. Compared to a single peak—which is realized in an IA chain with only one indepen-
63 dent degree of freedom in the unit cell [23]—double peaks provide a frequency range with a
64 significantly higher spatial attenuation strength. These traits bring rise to band gaps that
65 can be both low, wide, and highly attenuating—all while keeping the unit cell size within
66 the subwavelength regime. Upon reduction to its canonical form, inertial amplification
67 is realized by introducing a classical inerter element into a locally resonant mass-in-mass
68 chain [24], as demonstrated by Kulkarni and Manimala [25] and Al Babaa et al. [26].
69 Since its introduction in 2007 by Yilmaz et al., the concept of inertial amplification in
70 phononic media has been attracting increasing attention among the phononics commu-
71 nity; see, e.g., Refs. [22, 27–31].

72 In previous studies of inertially amplified (IA) phononic materials/structures, the dou-
73 ble peaks in the attenuation spectrum stem from a direct connection between an IA mass
74 (which exhibits an antiresonance) and an independent degree of freedom associated with
75 another component in the system causing the generation a second antiresonance (possibly

76 due to a local resonance effect).¹ This enables combined frequency breadth and spatial
 77 attenuation strength for the band gap, whereas the location of the IA antiresonance is
 78 determined by the level of amplification—which in turn is controlled by leveraging the ac-
 79 celeration of the IA mass using a rigid, or rigid-like, link. These features create an IA
 80 mechanism that either define the backbone configuration of a phononic waveguide [19–21]
 81 or serve as an attachment to a standard continuous elastic structure such as a rod [22]
 82 or a beam [28]. In the latter cases, the IA modal mass is coupled to a modal degree
 83 of freedom representing the motion of the supporting continuous base. In contrast, in
 84 this paper we present a mechanism whereby the generation of the double-peak attenua-
 85 tion band gap is obtained from a modal coupling of an IA mass and a locally resonant
 86 mass *separately attached* to the base waveguide. This intrinsic and coupled mixing of the
 87 motion of an IA mass and that of a conventional attached local resonator to open up
 88 a wide subwavelength band gap with two peaks in the imaginary wavenumber domain
 89 represents a novel concept with significant implications on band-gap design. We present
 90 a lumped-parameter model realising this concept, and derive the corresponding complex
 91 dispersion relation. An analytical expression is also provided that characterizes the cou-
 92 pling conditions. A parametric analysis is then carried out to identify the sensitivity of
 93 the governing parameters on the attenuation properties. Three metrics are proposed for
 94 quantifying the performance of this type of band gap. The behavior of these performance
 95 metrics with variation in the governing design parameters are then examined to pave the
 96 way for realization of optimized configurations. Effective mass and stiffness properties are
 97 also calculated to add further insight. Finally, we present at the end of our investigation
 98 a direct comparison—on both infinite and finite chains—between the response when the
 99 resonator mass is included versus when it is removed.

100 2. Mathematical modelling of the proposed inertial amplifier chain

101 Our proposed inertially amplified chain is depicted in Fig. 1(a). Two successive base-
 102 line masses M are connected to each other with a baseline spring K and a pair of inertial
 103 amplifiers each of mass m_a . Each inertial amplifier mass is levered with rigid links as
 104 illustrated in Fig. 1. These inertial amplifier masses play the key role in inducing inertial
 105 amplification, as their accelerations are amplified owing to the lever-arm formed by the
 106 connecting mechanism. To introduce a “tuning knob” for the level of inertial amplification,
 107 a vertical spring with stiffness k_a , termed the vertical stiffness of the inertial amplifier, is
 108 introduced as shown in Fig. 1(b). When the value of k_a is set to zero, maximum inertial
 109 amplification is attained. As it is increased, the level of inertial amplification decreases
 110 representing an effective loss of rigidity in the connecting link. In the limit of high vertical
 111 stiffness, the levered masses transition their behaviour to standard local resonance (see
 112 analysis in the following section).

¹This appears in both IA materials (represented by infinite models) [22] and IA structures (represented by finite models) [20–22].

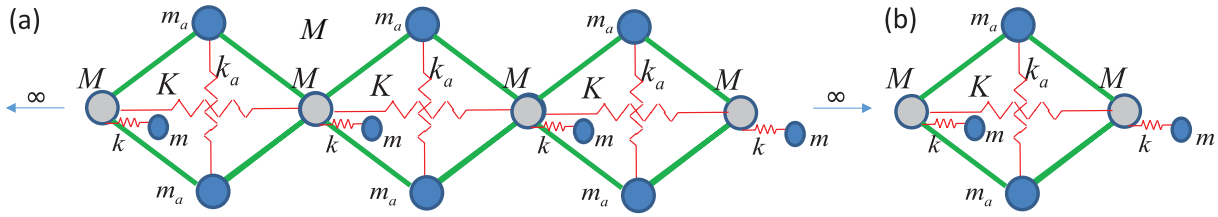


Fig. 1. (a) Proposed IA chain comprising a levered mass and a locally resonant mass. (b) A single representative unit cell.

2.1. Effective mass formulation for the tuning mass attached to the baseline chain

As mentioned above, a spring-mass linear resonator is attached to the base chain. The modal degree of freedom associated with the linear spring-mass resonator may be tuned to couple with that associated with the inertially amplified mass and thus creating a band gap with a double-attenuation peak in the imaginary part of the dispersion diagram; this aspect is discussed and analysed in the next sections. First we will examine the effective mass stemming from this unique configuration. The equation of motion of the resonating mass can be written as

$$m\ddot{w}_x + k(w_x - u_n) = 0 \quad \text{or} \quad w_x = \frac{1}{1 - \left(\frac{\omega^2}{\omega_s^2}\right)} u_n = \frac{1}{1 - \left(\frac{\omega^2 \omega_s^2}{\omega_s^2 \omega_r^2}\right)} u_n \quad \text{or} \quad w_x = \frac{1}{1 - \frac{\Omega^2}{\eta_r^2}} u_n, \quad (1)$$

where u_n and w_x denote the displacement of the baseline mass and local resonator mass, respectively, ω is the free wave frequency, $\omega_s^2 = K/M$ is the natural frequency of the base chain mass/spring, $\omega_r^2 = k/m$ is the natural frequency of the local resonator mass/spring, Ω is a non-dimensional frequency ratio defined as $\Omega = \omega/\omega_s$, and η_r is a non-dimensional frequency ratio which can be written as $\eta_r = \omega_r/\omega_s$.

The frequency dependent effective baseline mass M_e can be computed from the momentum balance as follows:

$$M_e \dot{u}_n = m \dot{w}_x + M \dot{u}_n \quad \text{or} \quad M_e = M \underbrace{\left(1 + \frac{\theta_r}{1 - \left(\frac{\Omega}{\eta_r}\right)^2} \right)}_{\chi_m}, \quad (2)$$

where $\theta_r = m/M$ is defined as a dimensionless parameter.

2.2. Force on the main mass from inertial amplifier

From the system kinematics, the relationship between the acceleration of the auxiliary masses \ddot{v}_n and the acceleration of the main mass \ddot{u}_n and \ddot{u}_{n-1} can be expressed as

$$v_n = \frac{(u_n - u_{n-1})}{2} \cot \alpha \quad \text{or} \quad \ddot{v}_n = \frac{(\ddot{u}_n - \ddot{u}_{n-1})}{2} \cot \alpha, \quad (3)$$

where α is the angle of the rigid-link with the axial axis of the base chain, as shown in Fig. 1. The force on the rigid links can be calculated by balancing the forces acting at

134 the mass of the inertial amplifier as

$$2F_n \sin \alpha = m_a \ddot{v}_n + 2k_a v_n \quad \text{or} \quad F_n = \frac{(-\omega^2 m_a + 2k_a)(u_n - u_{n-1})}{4 \sin \alpha \tan \alpha}. \quad (4)$$

135 The force component acting from the inertial amplifier on the baseline mass in the direc-
136 tion of the wave propagation is

$$\tilde{F}_n = 2F_n \cos \alpha = \underbrace{\frac{(-\omega^2 m_a + 2k_a)}{2 \tan^2 \alpha}}_{\chi} (u_n - u_{n-1}). \quad (5)$$

137 2.3. Equation of motion of the overall chain

138 The governing equation of motion for the n^{th} baseline mass in the chain is as follows:

$$\begin{aligned} M_e \ddot{u}_n + K(2u_n - u_{n-1} - u_{n+1}) + \tilde{F}_n - \tilde{F}_{n+1} &= 0, \\ \text{or} \quad (-\omega^2 M_e + 2K_e) u_n - K_e u_{n+1} - K_e u_{n-1} &= 0, \end{aligned} \quad (6)$$

139 where M_e and K_e are the effective baseline mass and stiffness of the overall chain as shown
140 in Fig 1. The effective stiffness K_e can be expressed as $K + \chi$ where χ is defined as shown
141 in Eq. 5. From Bloch's theorem, the displacement of the successive units can be written
142 as:

$$u_{n+1} = u_n e^{i\mu} \quad \text{and} \quad u_{n-1} = u_n e^{-i\mu}, \quad (7)$$

143 where a is the length of the unit cell, q is the wavenumber, and a dimensionless term qa
144 is represented by μ . Substituting Eq. 7 into Eq. 6, we derive the dispersion relationship
145 as

$$\begin{aligned} (-\omega^2 M_e + K_e (2 - e^{i\mu} - e^{-i\mu})) u_n &= 0 \quad \text{or} \quad \frac{\omega^2 M_e}{K_e} = 2(1 - \cos \mu) \\ \text{or} \quad \mu &= \cos^{-1} \left(1 - \frac{\omega^2 M_e}{2K_e} \right), \end{aligned} \quad (8)$$

146 The effective stiffness K_e , in turn, reads as

$$K_e = K + \frac{(-\omega^2 m_a + 2k_a)}{2 \tan^2 \alpha} = K + \frac{k_a}{2 \tan^2 \alpha} \left(2 - \frac{\Omega^2}{\eta_a^2} \right) = K (1 + \beta (2\eta_a^2 - \Omega^2)). \quad (9)$$

147 where

- 148 • $\beta = \frac{\theta}{2 \tan^2 \alpha} = \frac{m_a}{2M \tan^2 \alpha}$ is the inertial amplification factor; it is a parameter that rep-
149 represents the ratio of the inertial amplifier mass m_a to the baseline mass M considering
150 the influence of the angle of the inertial amplifier α . The parameter $\theta = m_a/M$ is
151 the ratio of the inertial amplifier mass to the baseline mass.
- 152 • $\eta_a = \omega_a/\omega_s$ is the ratio of the inertial amplifier/vertical spring natural frequency
153 $\omega_a = \sqrt{k_a/m_a}$ to the base chain mass/spring natural frequency $\omega_s = \sqrt{K/M}$.
- 154 • $\theta_r = m/M$ is the ratio of the resonator mass to the base chain mass.
- 155 • $\eta_r = \omega_r/\omega_s$ is the local resonator frequency ratio, defined as the ratio of the local
156 resonance mass/spring natural frequency $\omega_r = \sqrt{k/m}$ to the base chain mass/spring
157 natural frequency $\omega_s = \sqrt{K/M}$.

158 2.4. Band gaps

159 A propagation band may be identified from the range of $\cos \mu$ of Eq. 8; this is because
160 a real μ corresponds to a propagating wave:

$$-1 \leq \cos \mu \leq 1 \quad \text{or} \quad 0 \leq \frac{\omega^2 M_e}{K_e} \leq 4 \quad \text{or} \quad 0 \leq \frac{\Omega^2 \left(1 + \frac{\theta_r \eta_r^2}{\eta_a^2 - \Omega^2}\right)}{1 + \beta(2\eta_a^2 - \Omega^2)} \leq 4 \quad (10)$$

161 It can be seen that Eq. 10 depends only on four non-dimensional parameters: β , η_a , η_r
162 and θ_r . For $\eta_a = 0$, the inequality of Eq. 10 can be further simplified as follows:

$$\text{Propagating waves: } \begin{cases} 0 \leq \Omega \leq \Omega_{c1} || \Omega_{c2} \leq \Omega \leq \eta_r \sqrt{1 + \theta_r} & \text{if } \eta_r^2 > \frac{1}{\beta(1 + \theta_r)} \\ \eta_r \sqrt{1 + \theta_r} \leq \Omega \leq \sqrt{\frac{1}{2} (\epsilon_1 + \sqrt{\epsilon_2})} & \text{if } 0 < \eta_r^2 < \frac{1}{\beta(1 + \theta_r)} \end{cases} \quad (11)$$

163 where $\Omega_{c1} = \sqrt{\frac{1}{2} (\epsilon_1 - \sqrt{\epsilon_2})}$, $\Omega_{c2} = \sqrt{\frac{1}{2} (\epsilon_1 + \sqrt{\epsilon_2})}$, $\epsilon_1 = 4 + \eta_r^2(1 + 4\beta + \theta_r)/1 + 4\beta$,
164 and $\epsilon_2 = 16 - 8\eta_r^2(1 + 4\beta - \theta_r) + \eta_r^4(1 + 4\beta + \theta_r)^2/(1 + 4\beta)^2$. Equation 11 allows us to
165 indirectly predict the locations of the band-gap edges as a function of the model design
166 parameters.

167 2.5. Effective medium properties

168 Equation 2 and Eq. 9 define the frequency-dependent dynamical effective mass and
169 stiffness needed to obtain identical dispersive behavior. The effective mass ratio \bar{M} is the
170 ratio of the effective mass M_e to the baseline mass M , and the effective stiffness ratio \bar{K}
171 is the ratio of the effective stiffness K_e to the baseline stiffness K . These are expressed,
172 respectively, as follows:

$$\bar{M} = \frac{M_e}{M} = \left(1 + \frac{\theta_r}{1 - \left(\frac{\Omega}{\eta_r}\right)^2}\right) \quad \text{or} \quad \bar{K} = \frac{K_e}{K} = (1 + \beta(2\eta_a^2 - \Omega^2)). \quad (12)$$

173 In principle, a one-to-one mapping can be realized between the complex dispersion relation
174 and these frequency-dependent effective properties. These quantities will be used in the
175 upcoming subsection in the analysis of the attenuation mechanisms.

176 2.6. Formation mechanism of double-peak attenuation

177 Two attenuation peaks are noticed when the effective stiffness is equal to zero, i.e.,
178 $\bar{K} = 0$ and the effective mass tends to infinite, i.e., $M_e \rightarrow \infty$. From Eq. 12, it can be seen
179 that the stiffness peak Ω_s occurs at $\Omega_s = \sqrt{1/\beta}$ while $\eta_a = 0$ and the mass peak occurs
180 at $\Omega_m = \eta_r$. Additionally, the above condition occurs while a transition of the band-gap
181 character occurs at $\beta\eta_r^2(1 + \theta_r) = 1$.

183 2.7. Analysis of a finite IA chain

184 In conjunction to Bloch wave propagation analysis of infinite models, it is useful to

185 also examine the response of corresponding finite models. This provides insights into how
 186 the wave attenuation characteristics displayed in the imaginary wave number of the dis-
 187 persion diagrams manifest in a truncated finite system subject to some form of excitation.
 188 Implementing the “backward substitution based” method [15] and “momentum balance”
 189 technique [32] for a full finite chain, the transmittance and effective mass can be computed
 190 by the following approach. The displacement amplitude of the last unit cell in the finite
 191 chain is written as:

$$u_{n-1} = \underbrace{\frac{-\omega^2 M_e + K_e}{K_e}}_B u_n, \quad (13)$$

192 whereas, the displacement amplitude of the j^{th} unit cell is expressed as:

$$u_{j-1} = \underbrace{\frac{-\omega^2 M_e + 2K_e}{K_e}}_A u_j - u_{j+1}. \quad (14)$$

193 Solving Eq. 14 for the $n - 1$ and proceeding backwards to the second unit cell, we
 194 obtain the amplitude of displacement u_1 in terms of u_n . Thus, the transmittance can
 195 be easily expressed as $\tau = \log_{10} \left(\frac{u_1}{u_n} \right)$. The effective mass, on the other hand, can be
 196 computed as:

$$M_e^{\text{fin}} u_n = \sum_{j=2}^n M_e u_j \rightarrow M_e^{\text{fin}} = \frac{M_e^{\text{fin}}}{n M_e} = \frac{1}{n} \sum_{j=2}^n \frac{u_j}{u_n}. \quad (15)$$

197 3. Results and Discussion

198 In this section, we evaluate the dispersion relations derived and present their behaviour
 199 as a function of the model parameters with a focus on the influence on the attenuation
 200 profile in the imaginary part of the band structure diagram.

201 3.1. Variation of the non-dimensional design parameter β

202 We start by examining the variation of the inertial amplification factor β , which as
 203 described earlier is a function of the ratio θ of inertial amplifier mass m_a to baseline mass
 204 M and the rigid-link angle α . This parameter provides a direct representation of the
 205 level of effective inertial amplification of the levered mass—which in the static state is
 206 m_a —due to variation of the lever angle α . The effect of varying β on the dispersion and
 207 attenuation strength generates a multi-dimensional relationship that is plotted in Fig. 2.
 208 It is observed that the value of β drastically increases with decreasing angle α and linearly
 209 increases with the mass ratio. For example, for $\theta = 0.25$, an angle of $\alpha = 20^\circ$ matches
 210 roughly with $\beta = 1$. On the other hand, when α is lowered to only 12° or less, the inertial
 211 amplification factor jumps to 3 and higher. The factor $2 \tan^2 \alpha$ in the denominator in the
 212 definition of β (see Section 2.3) determines the level of inertial amplification beyond the
 213 static value of m_a . Next, we consider several parametric scenarios exploring limiting cases
 214 for the inertially amplified chain.

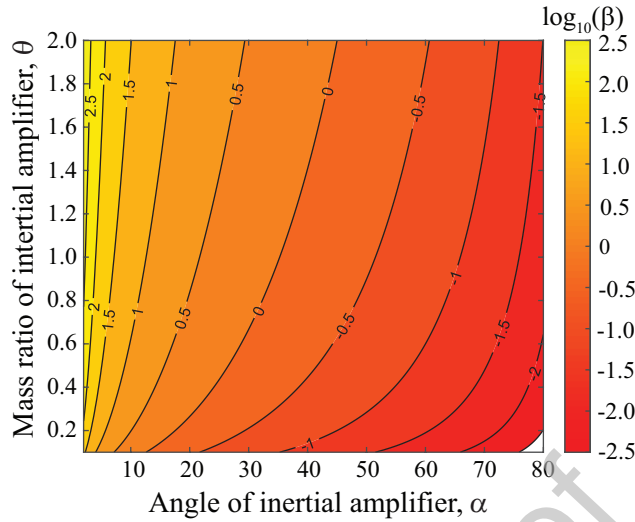


Fig. 2. Variation of the non-dimensional parameter β as a function of the ratio of the inertial amplifier mass to the baseline mass θ and the lever angle α

215 3.2. Case 1: No local resonator attached to baseline mass

216 First, we consider a case with only the inertial amplifier and no local resonator attached
 217 to the baseline mass; this configuration has been examined in Ref. [19]. This case is
 218 obtained by setting $\theta_r = 0$. Therefore, Eq. 10 can be simplified further to

$$0 \leq \Omega \leq 2\sqrt{\frac{1 + 2\beta\eta_a^2}{1 + 4\beta}}. \quad (16)$$

219 Thus, the attenuation band exists while $\Omega > 2\sqrt{\frac{1 + 2\beta\eta_a^2}{1 + 4\beta}}$ whereas the upper limit of the
 220 transmission band is restricted to $\Omega < 2$. The shifting of the attenuation band towards
 221 lower frequencies can be represented by

$$\varrho = \left(1 - \sqrt{\frac{1 + 2\beta\eta_a^2}{4\beta + 1}}\right) \times 100\%. \quad (17)$$

222 Here we conclude that the inertial amplifier mass, in the absence of the discrete local res-
 223 onator, creates only a single attenuation peak in the imaginary wavenumber part of the
 224 disperison diagram. While this configuration provides a semi-infinite attenuation profile
 225 above the IA antiresonance, the strength of this leveled attenuation (i.e., the maximum
 226 value of the imaginary wave number as the frequency goes to infinite) is relatively weak.

227

228 *Edge frequencies and dispersion relationship* The transmission band is extended from 0 to
 229 the edge frequency $\Omega_c = 2\sqrt{(1 + 2\beta\eta_a^2)/(1 + 4\beta)}$. The edge frequency is highly sensitive
 230 to two key non-dimensional parameters of the system, namely, the effective mass β and the
 231 frequency ratio η_a . The variation of the edge frequency in terms of β and η_a is illustrated

232 in Fig. 3(b). In Fig. 3(a), the concise dispersion diagram for the system having an inertial
 233 amplifier mass ratio of $\beta = 1$ and frequency ratio $\eta_a = 0, \sqrt{2}$ and 2 are plotted. It is
 234 noticed that a rise in η_a increases the width of the low-frequency propagation band. The
 235 edge frequency Ω_c decreases with increasing β when $\eta_a < \sqrt{2}$ and vice-versa.

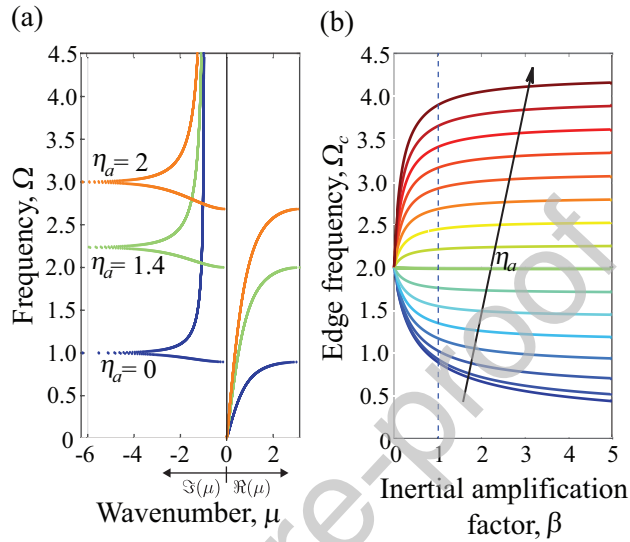


Fig. 3. (Left) Dispersion diagram for $\beta = 1$ and three different values of η_a : $0, \sqrt{2}$ and 2. (Right) Variation of the band-gap edge frequency Ω_c in terms of β for different values of η_a

236 3.3. Case 2: Flexible inertial amplifier with a local resonator attached to the baseline mass

237 Now, a conventional local resonant mass m is attached to the baseline mass M of the
 238 chain; we will occasionally refer to this as the “tuning” mass. First, the coefficient of the
 239 vertical spring supporting the inertial amplifier—which in practice may be viewed as a
 240 representation of the actual stiffness of the joints—is assumed to be $k_a = 0$, which means
 241 the frequency ratio of the inertial amplifier is also 0.

242 3.3.1. Dispersion relations

243 The complex dispersion diagram including both propagation and attenuation bands
 244 (with the strength of the latter indicated by the absolute value in the imaginary wavenum-
 245 ber domain) is computed from Eq. 8. The effects of the inertial amplifier mass ratio β ,
 246 the resonator natural frequency ratio η_r , and the resonator mass ratio θ_r on the overall

247 dispersion curves, specifically the attenuation profile, are examined closely in this section.

Figures 4, 5, and 6 illustrate the impact on the attenuation profile with varying β , η_r and

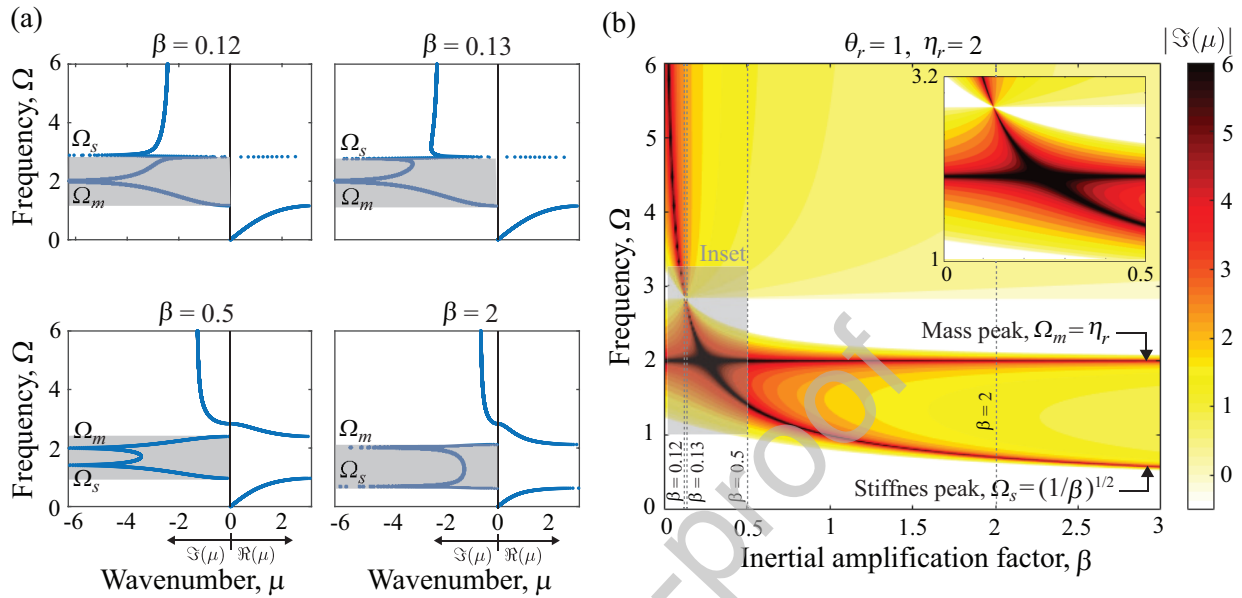


Fig. 4. Effect of the non-dimensional design parameter β on the complex band structure. (a) Dispersion diagrams for four different values of β . (b) Attenuation profile (represented by the normalized imaginary wave number) as a function of frequency Ω and β . For $\beta = 0.12$, the attenuation profile exhibits two uncoupled peaks, the lower one corresponding to a standard local resonance and the higher one representing an IA antiresonance. For $\beta = 0.12$, transition has occurred to an attenuation profile with two coupled peaks. The distance in the frequency domain between the two coupled attenuation peaks is observed to grow with further increase in β . All results are for a vertical stiffness $k_a = 0$, i.e., $\eta_a = 0$.

248

249 θ_r , respectively. From Fig. 4, the following observations are noted:

- 250 • With increase in inertial amplifier mass ratio β , the IA band gap widens and its
251 central frequency drops to lower values.
- 252 • The two attenuation peaks, namely mass peak Ω_m and stiffness peak Ω_s are located
253 where the effective mass and effective stiffness of the medium turns to infinite and
254 zero respectively. Only the stiffness peak shifts to the low frequency side and the
255 mass peak remains constant while β is increased.
- 256 • Below a cut off value in β , defined as $\beta^* = \frac{1}{\eta_r^2(1+\theta_r)}$, the double-peak IA attenuation
257 phenomenon cannot be observed. In particular, for $\beta = 0.12$, we notice that the
258 IA antiresonance peak is not coupled with the attenuation peak associated with the

259 local resonance of the tuning mass at $\eta_r = 2.0$. However, for higher values of β these
 260 two attenuation peaks couple and generate a relatively large IA band gap with these
 261 two peaks appearing inside the band gap.

- 262 • A "four-legged" focal point is identified in the β contour diagram indicating a region
 263 of maximum attenuation strength. This point is located where $\Omega_s = \Omega_m$.

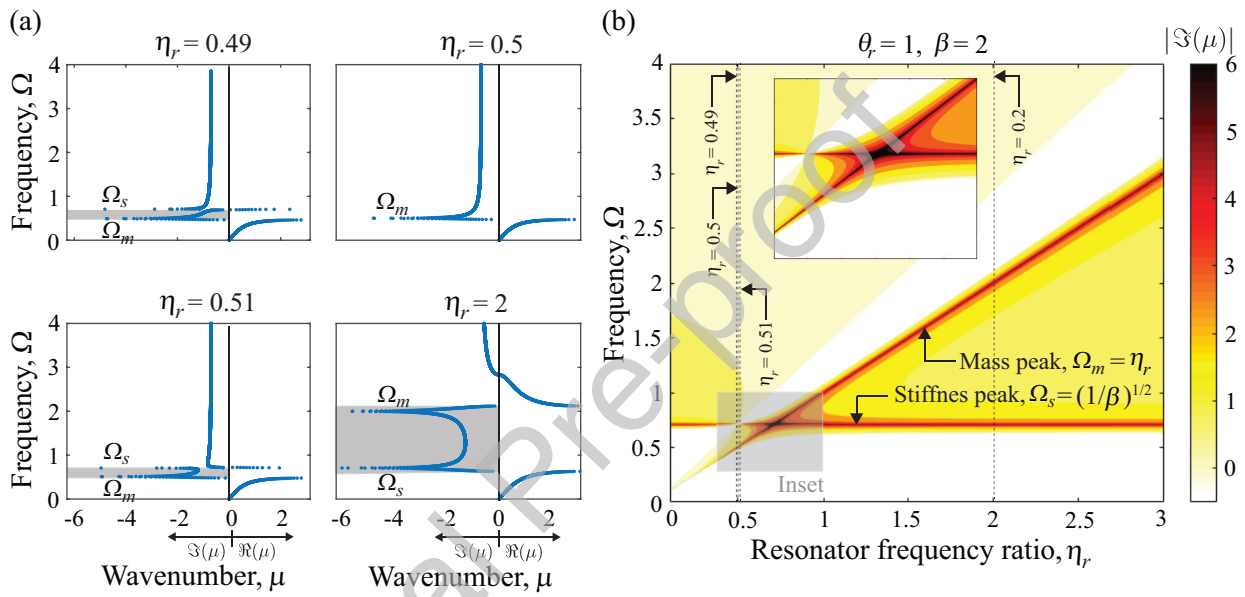


Fig. 5. Effect of the natural frequency ratio η_r on the complex band structure. (a) Dispersion diagrams for four different values of η_r . (b) Attenuation profile (represented by the normalized imaginary wave number) as a function of frequency Ω and η_r . For $\eta_r = 0.49$ the attenuation profile exhibits two uncoupled peaks, the lower one corresponding to a standard local resonance and the upper one representing an IA antiresonance. For $\eta_r = 0.5$, transition has occurred to an attenuation profile with two coupled peaks. The distance in the frequency domain between the two coupled attenuation peaks is observed to grow with further increase in η_r . All results are for a vertical stiffness $k_a = 0$, i.e., $\eta_a = 0$.

264 As for Fig. 5, it illustrates the following:

- 265 • The IA band gap width increases with the resonator natural frequency ratio η_r
 266 beyond a transitional value of $\eta_r = 0.5$; below this value the chain behaves mostly
 267 like a conventional locally resonant chain.
- 268 • The location of the mass peak varies with the natural frequency ratio of resonator;
 269 however, the stiffness peak remains constant.

- 270 • At $\eta_r = 0.5$, the transition point, the attenuation due to the stiffness peak vanishes
 271 and a single attenuation peak (mass peak) in the dispersion diagram is noticed.
- 272 • At that transitional value, the resonance due to the tuning mass and the inertial
 273 amplifier mass matches and a cross-over occurs.

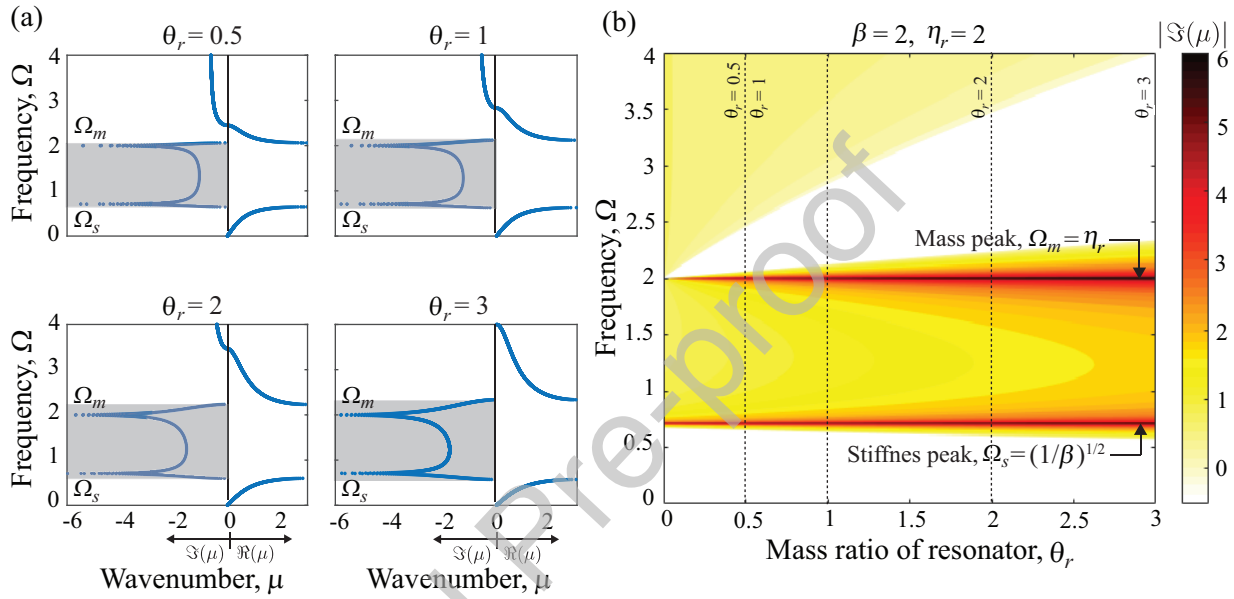


Fig. 6. Effect of the mass ratio θ_r on the complex band structure. (a) Dispersion diagrams for four different values of θ_r . (b) Attenuation profile (represented by the normalized imaginary wave number) as a function of frequency Ω and θ_r . For all values of θ_r considered, the attenuation profile exhibits two coupled peaks. The distance in the frequency domain between the two coupled attenuation peaks is observed to stay nearly constant with further increase in θ_r . All results are for a vertical stiffness $k_a = 0$, i.e., $\eta_a = 0$.

274 Unlike the previous two cases, the IA band gap and the frequency of the two peaks
 275 remain practically constant when the tuning mass ratio θ_r is varied; however, the level
 276 of attenuation increases with increasing θ_r , as shown in Fig. 6. The tuning mass may
 277 be made to have a more influential effect by changing other parameters in the system as
 278 shown below.

279 3.3.2. Metrics for band-gap size and attenuation performance

280 To quantify the properties of an IA band gap with double attenuation peaks, three
 281 metrics are proposed as shown in Fig. 7. The metric μ_{min} denotes the minimum level of

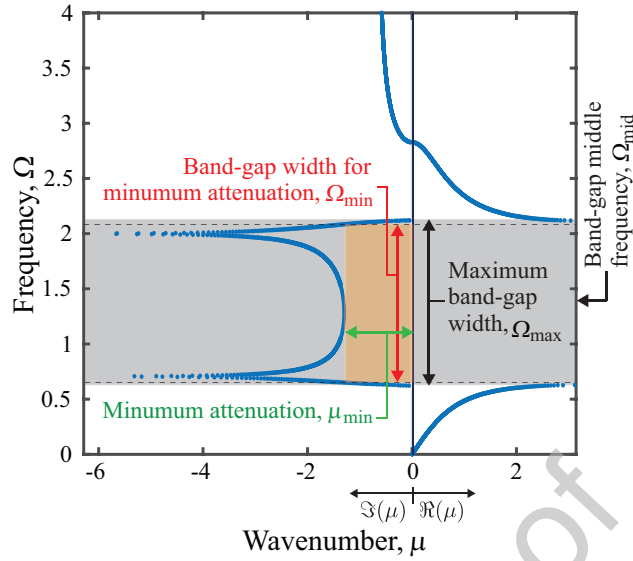


Fig. 7. Illustration of three metrics for the quantification of the relative band-gap size, minimum attenuation level, and relative band gap size corresponding to the minimum attenuation level.

282 attenuation achieved within the IA band gap within the frequency range Ω_{\min} as illustrated
 283 in the figure. As for the metric Ω_{\max} , this represents the conventional band-gap width. In
 284 both frequency metrics, the bandwidth is normalized with respect to its central frequency
 285 value, ω_{mid} . Upon normalization, Ω_{\min} and Ω_{\max} are denoted Ω_{\min}^* and Ω_{\max}^* , respectively.
 286 The variation of the metrics as a function of each of β , η_r , and θ_r is plotted in Fig. 8.
 287 Figures 8(a) and 8(b) illustrate that an IA band gap exists after certain cut-off values
 288 of β and η_r , respectively. With increasing β and η_r , beyond certain values, a wider IA
 289 band gap is possible at the cost of low level of attenuation μ_{\min} . In contrast, all metrics
 290 monotonically increase with θ_r . We observe in Fig. 8(b) that compared to when $m = 0$, a
 291 design with a relatively elevated level of minimum attenuation over practically the entire
 292 width of the band gap is possible for a band gap with a relative width of 130%. In
 293 contrast, a design is possible with a 15-fold increase in μ_{\min} but with a relatively smaller
 294 band-gap size. These results show a trade-off between large band-gap size and minimum
 295 attenuation strength. The regions shaded in green in Fig. 8 represent the net “gain” in
 296 minimum attenuation strength due to the addition of the locally resonant mass and the
 297 consequent generation of the coupled double-peak band gap.

298 The addition of a locally resonant mass, on the other hand, increases the total weight
 299 of the unit cell; this represents a design challenge when there is a constraint on the
 300 total weight. Future investigations may explore optimization studies with the additional
 301 constraint of keeping the total mass within the unit cell fixed.

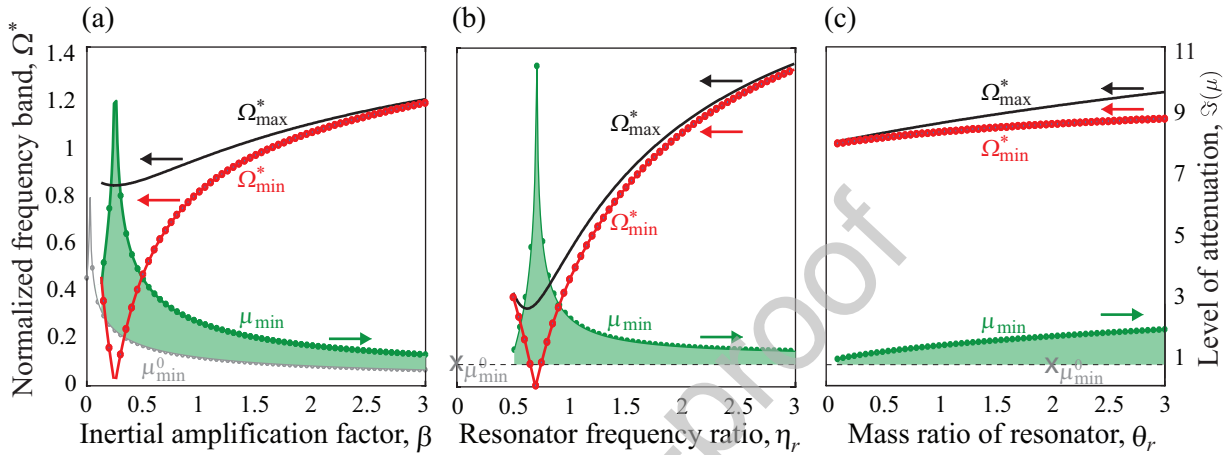


Fig. 8. Variation of the band-gap and attenuation metrics with respect to (a) β , (b) η_{r1} , and (c) θ_{r1} while keeping $\eta_a = 0$.

3.4. Inertial amplification with vertical spring with varying stiffness

302 To determine the effect of the vertical spring stiffness k_a on the IA band gap and
 303 attenuation profile, the inertial amplifier natural frequency ratio η_a is varied; this is shown
 304 in the form of the complex dispersion diagram in the top panel of Fig. 9. A contour plot
 305 of the attenuation level as a function of the inertial amplification factor β for the different
 306 η_a values is plotted in the lower panel of Fig. 9. This figure depicts that as k_a increases,
 307 i.e., η_a no longer remains 0, the IA band gap shifts towards higher frequencies. And,
 308 critically, when $\eta_a > \eta_{r1}$, the IA band-gap character is lost and the chain behaves mostly
 309 like a conventional locally resonance chain. Therefore, a lower value of k_a is desirable to
 310 realize a wider and lower-frequency IA band. This underlies the importance of having
 311 a quality lever, with maximum lever rigidity, minimal joint stiffness, etc., when realising
 312 this system in practice.

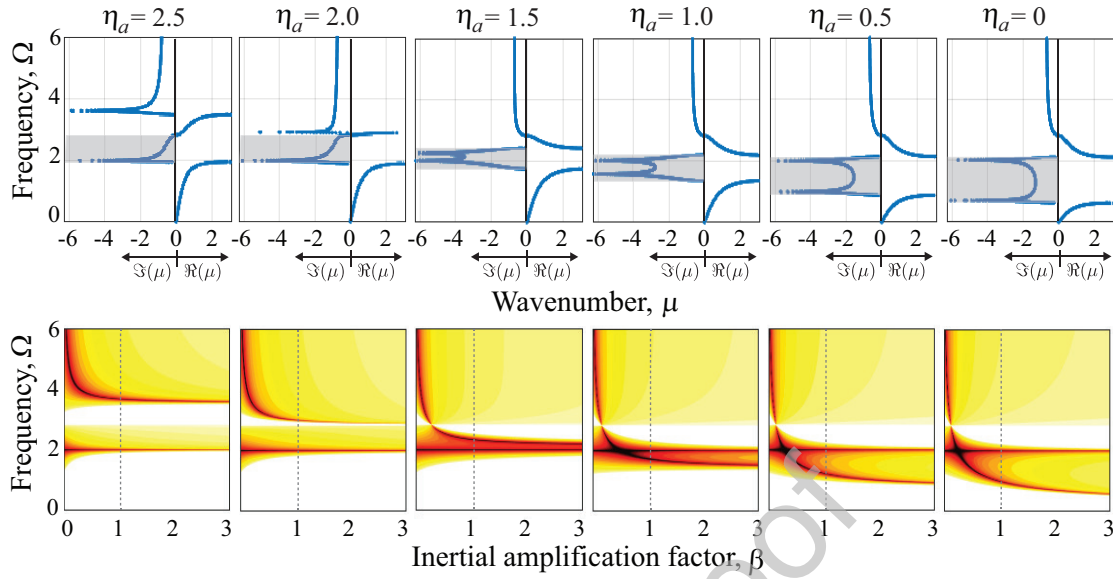


Fig. 9. Band-gap attenuation characteristics as a function of vertical stiffness for the range $\eta_a = 2.5$ to $\eta_a = 0$ (left to right) with an interval of $\Delta\eta_a = 0.5$

3.5. Effective properties of the overall elastic waveguide

Finally, we show that for our proposed inertial amplifier chain, the frequency-dependent dynamic effective mass and effective stiffness exhibit a rich set of properties that vary qualitatively with the key design parameters β , η_r , and θ_r . Specifically, negative effective mass, negative effective stiffness, and dual negative mass and stiffness behavior are realized as indicated in Fig. 10. The following observations are made:

- The dynamic effective stiffness becomes negative over a broad region in the top-right corner of the $\Omega - \beta$ spectrum, in contrast to a narrow region in the $\Omega - \theta_r$ and $\Omega - \eta_r$ spectra.
- The dynamic effective stiffness becomes negative in a narrow region in the bottom-left corner of the $\Omega - \beta$ spectrum, in contrast to broad top-left and bottom-right regions in the $\Omega - \theta_r$ and $\Omega - \eta_r$ spectra.
- Attenuation bands generate in two scenarios:
 1. When either of the dynamic effective medium properties, mass or stiffness, turns negative, or

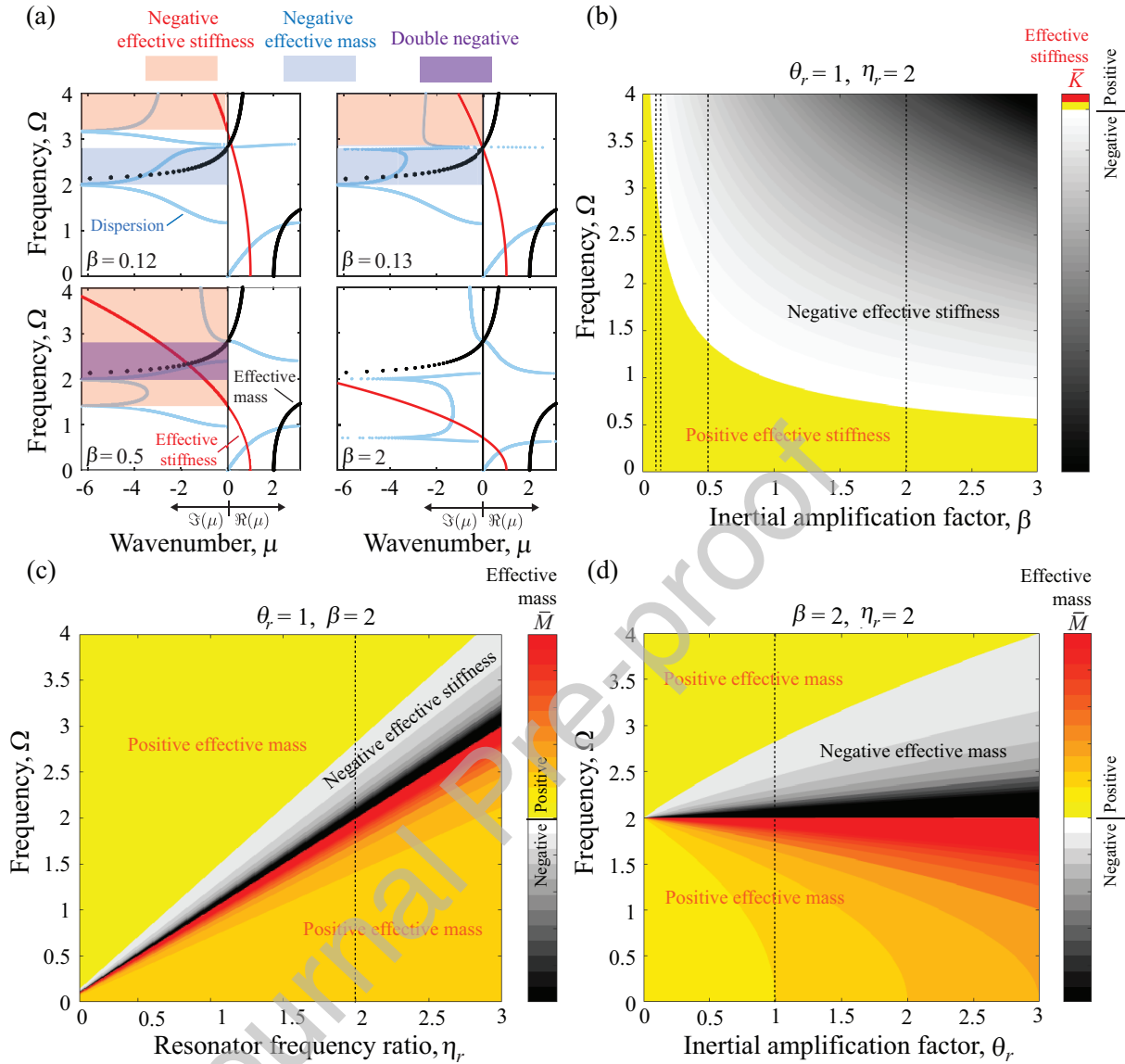


Fig. 10. Dynamic effective properties superimposed on the complex dispersion and corresponding contour plots

329 2. the inertial force of the effective medium becomes four times higher than the
 330 dynamic effective stiffness

331 • The local resonance attenuation peak corresponds to the dynamic effective mass
 332 tending to infinity (denoted as mass peak); and the IA attenuation peak corresponds
 333 to the dynamic effective stiffness tending to zero (denoted as stiffness peak).

334 • When these two attenuation peaks fall between the two edge frequencies, i.e., Ω_{c1}

335 and Ω_{c2} , coupled double-peak attenuation occurs.

- 336 • For the set of parameters for which the mass peak and stiffness peak coincide, a
337 significantly high level of attenuation is attained.
- 338 • A double negative region emerges where the dynamic effective mass and stiffness
339 are simultaneously negative [33, 34]. Observation of a double negative band in a
340 similar chain mode was reported in Ref. [35], although no reference was made on
341 the possibility of coupled peaks in the attenuation spectrum.

342 3.6. Transmittance and effective mass in truncated finite chain

343 The results illustrated in Fig. 11 provide confirmation that the attenuation characteris-
344 tics shown in all the complex dispersion diagrams presented carry over to a corresponding
345 10-unit cell long finite chain. We observe that the transmittance through a finite chain
346 significantly reduces in a manner that directly correlates with the attenuation in the
347 dispersion, with the two coupled attenuation peaks matching in their appearance. No-
348 ticeably, we observe that in absence of the attached resonator, the effective mass of the
349 system becomes frequency independent.

351 3.7. Future extensions to more complex coupled IA-local resonance configurations

352 The mass-spring-inertial amplifier configuration presented in Fig. 1 is a canonical con-
353 figuration that serves the purpose of providing a demonstration of the core concept of
354 coupling an IA antiresonance with an attenuation peak associated with a standard sepa-
355 rately attached local resonator. This cononical framework has enabled rigorous analytical
356 characterization and investigation of the concept. However, it is readily extendable to
357 more complex configurations in higher dimensions. For example, a quasi-1D configura-
358 tion comprising multiple interconnected layers of masses and springs could form the base
359 chain [36]. Realization using standard mechanical components such as rods and beams

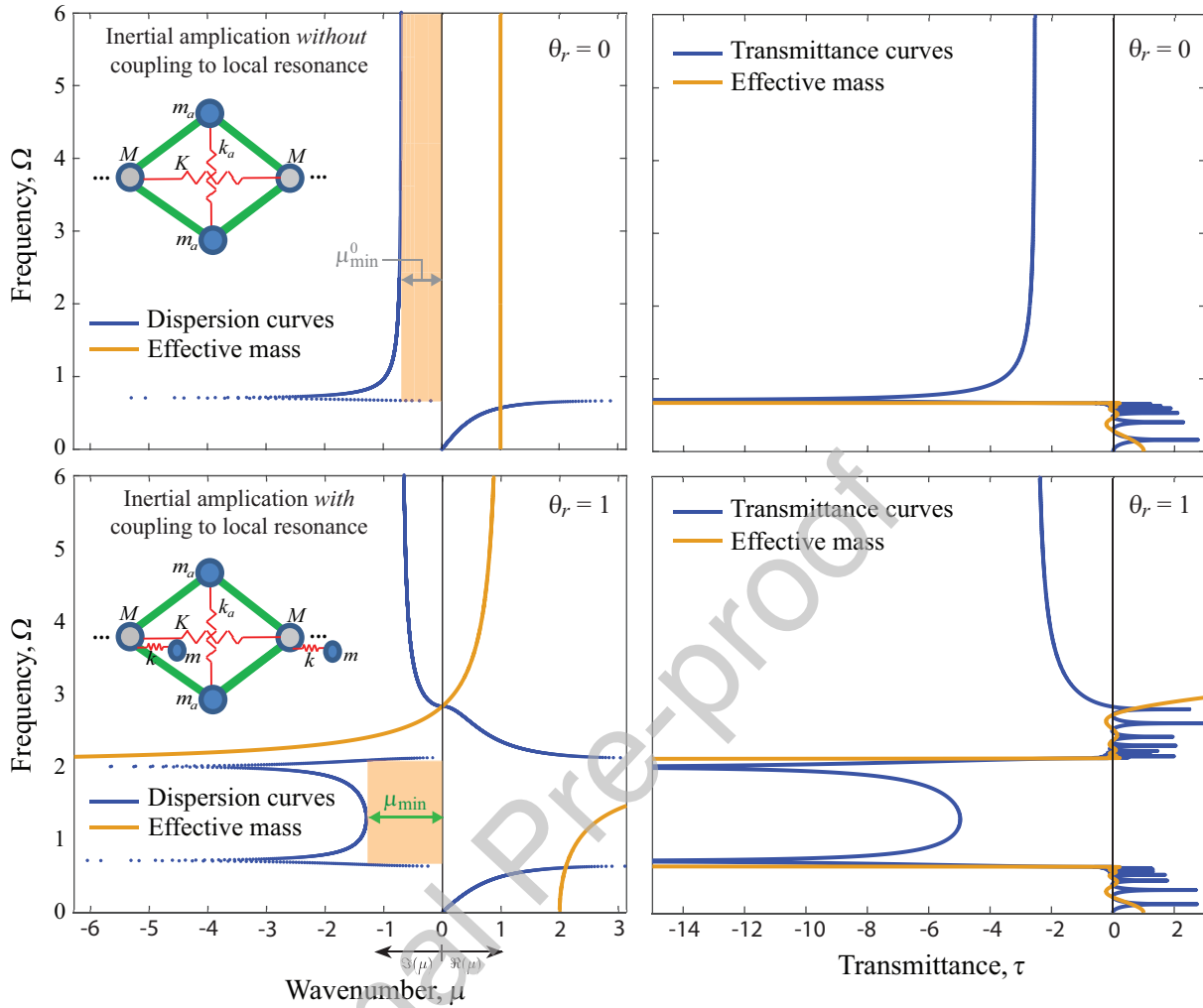


Fig. 11. Dispersion curves (blue; in wavenumber μ) and effective mass (orange; units omitted) for IA chain (a) without added local resonator, i.e. $\theta_r = 0$, and (b) with added local resonator having a mass ratio $\theta_r = 1$. Transmittance curves (blue; in transmittance τ) and effective mass (orange; units omitted) for a corresponding finite chain comprising ten units cells (c) without added local resonator, i.e., $\theta_r = 0$, and (d) with added local resonator having mass ratio $\theta_r = 1$.

360 is also possible [22, 28]. Extension to higher dimensions may also be explored by con-
 361 sidering, for example, a cage-type 2D [37] or 3D [38] structure to form the base medium
 362 from which levered substructures and separately attached local resonators could emerge.
 363 Incorporation of damping in the system—to yield metadamping behavior [39–42]—and/or
 364 nonlinearity [43–45] are also other promising future avenues of investigation.

4. Conclusions

A novel concept for the realization of an inertial amplification band gap with double attenuation peaks has been presented. The concept is based on coupling a mass that is inertially amplified by a lever arm with a secondary mass that is separately attached to the backbone chain. This secondary mass on its own represent a conventional local resonator that may be introduced to any system as a separate attachment. Upon tuning, the local resonance of this mass couples with the resonance associated with the inertially amplified mass leading to a low and wide IA band gap with a characteristic double peaks in the attenuation profile. Compared to a corresponding IA chain with only a single attenuation peak and a semi-infinite but weak attenuation profile at frequencies above this peak, here we get a spatial attenuation profile that is finite in its frequency range, but strong in its intensity. A key advantage is that the band-gap edge frequencies, width, and minimum attenuation strength may all be optimized through this coupled IA-local resonance configurational concept.

Given these favorable characteristics, we derived mathematical expressions for the conditions for transition to the double-peak coupled regime. Extensive mappings of the response were then provided to conceptualize the effects of key parameters in the chain, namely the inertial amplification factor, the resonator natural frequency ratio, and the local resonator mass ratio, on the band-gap location, size, and attenuation profile. Furthermore, a vertical spring supporting the inertial amplifier mass pair is introduced to quantify—from a practical perspective—the effect of the lever link stiffness (which in our model is treated as rigid) on the degree of inertial amplification as realized in the dynamical response. Finally, three IA band-gap metrics have been introduced to characterize the band-gap relative size and attenuation properties, and a parametric optimization study was conducted to elucidate the effects of the various chain parameters on these metrics. It is observed that complex relations unfold with changing the IA and local resonator masses; for example, the minimum attenuation strength experiences an optimal point

392 that coincides with the lowest relative band-gap size. These results pave the way for the
393 design of a new class of inertially amplified phononic materials with superior IA band-gap
394 performance characteristics.

395 *Acknowledgement:* AB acknowledges the Inspire faculty grant, grant number DST/
396 INSPIRE/04/2018/000052, for supporting the research.

397

398 *Data availability statement* The raw/processed data required to reproduce these findings
399 cannot be shared at this time due to technical or time limitations.

400 References

- 401 [1] D. J. Mead, Wave propagation in continuous periodic structures: Research contributions from
402 Southampton, 1964-1995, *Journal of Sound and Vibration* 190 (3) (1996) 495–524.
- 403 [2] M. I. Hussein, M. J. Leamy, M. Ruzzene, Dynamics of Phononic Materials and Structures: Historical
404 Origins, Recent Progress, and Future Outlook, *Applied Mechanics Reviews* 66 (4) (2014) 40802.
- 405 [3] A. Banerjee, R. Das, E. P. Calius, Waves in structured mediums or metamaterials: A review,
406 *Archives of Computational Methods in Engineering* 26 (4) (2019) 1029–1058.
- 407 [4] M. M. Sigalas, E. N. Economou, Elastic and acoustic wave band structure, *Journal of Sound and*
408 *Vibration* 158 (2) (1992) 377–382.
- 409 [5] M. S. Kushwaha, P. Halevi, L. Dobrzynski, B. Djafari-Rouhani, Acoustic band structure of periodic
410 elastic composites, *Physical Review Letters* 71 (13) (1993) 2022–2025.
- 411 [6] Z. Liu, X. Zhang, Y. Mao, Y. Y. Zhu, Z. Yang, C. T. Chan, P. Sheng, Locally Resonant Sonic
412 Materials, *Science* 289 (5485) (2000) 1734–1736.
- 413 [7] Y. Jin, Y. Pennec, B. Bonello, H. Honarvar, L. Dobrzynski, B. Djafari-Rouhani, M. Hussein, Physics
414 of surface vibrational resonances: Pillared phononic crystals, metamaterials, and metasurfaces, *Re-*
415 *ports on Progress in Physics*.
- 416 [8] O. Sigmund, J. Søndergaard Jensen, Systematic design of phononic band-gap materials and struc-
417 tures by topology optimization, *Philosophical Transactions of the Royal Society of London. Series*
418 *A: Mathematical, Physical and Engineering Sciences* 361 (1806) (2003) 1001–1019.
- 419 [9] O. R. Bilal, M. I. Hussein, Ultrawide phononic band gap for combined in-plane and out-of-plane
420 waves, *Physical Review E* 84 (6) (2011) 065701.
- 421 [10] Y. Lu, Y. Yang, J. K. Guest, A. Srivastava, 3-D phononic crystals with ultra-wide band gaps,

- 422 Scientific Reports 7 (1) (2017) 1–14.
- 423 [11] S. Jiang, H. Hu, V. Laude, Ultra-wide band gap in two-dimensional phononic crystal with combined
424 convex and concave holes, *Physica Status Solidi-Rapid Research Letters* 12 (2) (2018) 1700317.
- 425 [12] L. DAlessandro, R. Ardito, F. Braghin, A. Corigliano, Low frequency 3d ultra-wide vibration atten-
426 uation via elastic metamaterial, *Scientific reports* 9 (1) (2019) 1–8.
- 427 [13] O. R. Bilal, M. I. Hussein, Trampoline metamaterial: Local resonance enhancement by springboards,
428 *Applied Physics Letters* 103 (11) (2013) 111901.
- 429 [14] E. Coffy, T. Lavergne, M. Addouche, S. Euphrasie, P. Vairac, A. Khelif, Ultra-wide acoustic band
430 gaps in pillar-based phononic crystal strips, *Journal of Applied Physics* 118 (21) (2015) 214902.
- 431 [15] A. Banerjee, R. Das, E. P. Calius, Frequency graded 1D metamaterials: A study on the attenuation
432 bands, *Journal of Applied Physics* 122 (7) (2017) 075101.
- 433 [16] L. Liu, M. I. Hussein, Wave motion in periodic flexural beams and characterization of the transition
434 between Bragg scattering and local resonance, *Journal of Applied Mechanics* 79 (1) (2012) 11003–
435 11017.
- 436 [17] Z. Jia, Y. Chen, H. Yang, L. Wang, Designing phononic crystals with wide and robust band gaps,
437 *Physical Review Applied* 9 (4) (2018) 044021.
- 438 [18] Z. Liu, C. T. Chan, P. Sheng, Three-component elastic wave band-gap material, *Physical Review B*
439 65 (16) (2002) 165116.
- 440 [19] C. Yilmaz, G. M. Hulbert, N. Kikuchi, Phononic band gaps induced by inertial amplification in
441 periodic media, *Physical Review B* 76 (5) (2007) 54309.
- 442 [20] C. Yilmaz, G. M. Hulbert, Theory of phononic gaps induced by inertial amplification in finite
443 structures, *Physics Letters A* 374 (34) (2010) 3576–3584.
- 444 [21] G. Acar, C. Yilmaz, Experimental and numerical evidence for the existence of wide and deep
445 phononic gaps induced by inertial amplification in two-dimensional solid structures, *Journal of Sound
446 and Vibration* 332 (24) (2013) 6389–6404.
- 447 [22] N. M. M. Frandsen, O. R. Bilal, J. S. Jensen, M. I. Hussein, Inertial amplification of continuous
448 structures: Large band gaps from small masses, *Journal of Applied Physics* 119 (12) (2016) 124902.
- 449 [23] C. Yilmaz, G. M. Hulbert, Chapter 11: Dynamics of Locally Resonant and Inertially Amplified
450 Lattice Materials, in: A. S. Phani, M. I. Hussein (Eds.), *Dynamics of Lattice Materials*, John Wiley
451 Sons Ltd, 2017, pp. 233–258.
- 452 [24] H. Huang, C. Sun, G. Huang, On the negative effective mass density in acoustic metamaterials,
453 *International Journal of Engineering Science* 47 (4) (2009) 610–617.
- 454 [25] P. P. Kulkarni, J. M. Manimala, Longitudinal elastic wave propagation characteristics of inertant

- 455 acoustic metamaterials, *Journal of Applied Physics* 119 (24) (2016) 245101.
- 456 [26] H. Al Ba'ba'a, D. DePauw, T. Singh, M. Nough, Dispersion transitions and pole-zero characteristics
457 of finite inertially amplified acoustic metamaterials, *Journal of Applied Physics* 123 (10) (2018)
458 105106.
- 459 [27] S. Taniker, C. Yilmaz, Generating ultra wide vibration stop bands by a novel inertial amplification
460 mechanism topology with flexure hinges, *International Journal of Solids and Structures* 106 (2017)
461 129–138.
- 462 [28] J. Li, S. Li, Generating ultra wide low-frequency gap for transverse wave isolation via inertial
463 amplification effects, *Physics Letters A* 382 (5) (2018) 241–247.
- 464 [29] A. H. Orta, C. Yilmaz, Inertial amplification induced phononic band gaps generated by a compliant
465 axial to rotary motion conversion mechanism, *Journal of Sound and Vibration* 439 (2019) 329–343.
- 466 [30] A. Foehr, O. R. Bilal, S. D. Huber, C. Daraio, Spiral-based phononic plates: From wave beaming to
467 topological insulators, *Physical review letters* 120 (20) (2018) 205501.
- 468 [31] O. Yuksel, C. Yilmaz, Realization of an ultrawide stop band in a 2-D elastic metamaterial with topo-
469 logically optimized inertial amplification mechanisms, *International Journal of Solids and Structures*
470 203 (2020) 138–150.
- 471 [32] G. W. Milton, J. R. Willis, On modifications of Newton's second law and linear continuum elas-
472 todynamics, *Proceedings of the Royal Society A: Mathematical, Physical and Engineering Science*
473 463 (2079) (2007) 855–880.
- 474 [33] J. Li, C. T. Chan, Double-negative acoustic metamaterial, *Physical Review E* 70 (5) (2004) 055602.
- 475 [34] H. H. Huang, C. T. Sun, Anomalous wave propagation in a one- dimensional acoustic metamaterial
476 having simultaneously negative mass density and Youngs modulus, *The Journal of the Acoustical*
477 *Society of America* 132 (2012) 2887.
- 478 [35] X. Zhou, X. Liu, G. Hu, Elastic metamaterials with local resonances: an overview, *Theoretical and*
479 *Applied Mechanics Letters* 2 (4) (2012) 041001.
- 480 [36] Y. Li, X. Wang, G. Yan, Configuration effect and bandgap mechanism of quasi-one-dimensional
481 periodic lattice structure, *International Journal of Mechanical Sciences* 190 (2021) 106017.
- 482 [37] Y. Jin, Y. Shi, G.-C. Yu, G.-T. Wei, B. Hu, L.-Z. Wu, A multifunctional honeycomb metastructure
483 for vibration suppression, *International Journal of Mechanical Sciences* 188 (2020) 105964.
- 484 [38] W. Jiang, M. Yin, Q. Liao, L. Xie, G. Yin, Three-dimensional single-phase elastic metamaterial
485 for low-frequency and broadband vibration mitigation, *International Journal of Mechanical Sciences*
486 190 (2021) 106023.
- 487 [39] M. I. Hussein, M. J. Frazier, Metadamping: An emergent phenomenon in dissipative metamaterials,

- 488 Journal of Sound and Vibration 332 (20) (2013) 4767–4774.
- 489 [40] C. L. Bacquet, M. I. Hussein, Dissipation engineering in metamaterials by localized structural dy-
490 namics (2018) arXiv:1809.04509 [physics.app-ph].
- 491 [41] C. L. Bacquet, H. Al Babaa, M. J. Frazier, M. Nouh, M. I. Hussein, Chapter Two - Metadamping:
492 Dissipation Emergence in Elastic Metamaterials, in: M. I. Hussein (Ed.), *Advances in Applied*
493 *Mechanics*, Vol. 51, 2018, pp. 115–164.
- 494 [42] A. Aladwani, M. Nouh, Mechanics of metadamping in flexural dissipative metamaterials: Analysis
495 and design in frequency and time domains, *International Journal of Mechanical Sciences* 173 (2020)
496 105459.
- 497 [43] L. B. S., J. S. Jensen, Low-frequency band gaps in chains with attached non-linear oscillators,
498 *International Journal of Nonlinear Mechanics* 42 (2007) 1186–1193.
- 499 [44] R. Khajehtourian, H. M. I., Dispersion characteristics of a nonlinear elastic metamaterial, *AIP*
500 *Advances* 4 (2014) 124308.
- 501 [45] X. Xu, M. V. Barnhart, X. Fang, J. Wen, Y. Chen, G. Huang, A nonlinear dissipative elastic meta-
502 material for broadband wave mitigation, *International Journal of Mechanical Sciences* 164 (2019)
503 105159.

Elsevier instructions:

504

Author contributions

For transparency, we encourage authors to submit an author statement file outlining their individual contributions to the paper using the relevant CRediT roles: Conceptualization; Data curation; Formal analysis; Funding acquisition; Investigation; Methodology; Project administration; Resources; Software; Supervision; Validation; Visualization; Roles/Writing – original draft; Writing – review & editing. Authorship statements should be formatted with the names of authors first and CRediT role(s) following.

Authors' response:

Authors opt not to include an author statement.

Journal Pre-proof

505 **Declaration of interests**

The authors declare that they have no known competing financial interests or personal relationships that could have appeared to influence the work reported in this paper.

The authors declare the following financial interests/personal relationships which may be considered as potential competing interests:

Journal Pre-proof